entropy

MDPI

Article

A Numerical Study on Entropy Generation in Two-Dimensional Rayleigh-Bénard Convection at Different Prandtl Number

Yikun Wei [1,*,†], Zhengdao Wang [2,*,†] and Yuehong Qian [2]

[1] Faculty of Mechanical Engineering and Automation, Zhejiang Sci-Tech University, Hangzhou 310018, China
[2] Shanghai Key Laboratory of Mechanics in Energy Engineering, Shanghai University, Shanghai 200072, China; qian@shu.edu.cn
* Correspondence: ykun_wei@sina.com (Y.W.); dao527@126.com (Z.W.)
† These authors contributed equally to this work.

Received: 2 July 2017; Accepted: 21 August 2017; Published: 30 August 2017

Abstract: Entropy generation in two-dimensional Rayleigh-Bénard convection at different Prandtl number (*Pr*) are investigated in the present paper by using the lattice Boltzmann Method. The major concern of the present paper is to explore the effects of *Pr* on the detailed information of local distributions of entropy generation in virtue of frictional and heat transfer irreversibility and the overall entropy generation in the whole flow field. The results of this work indicate that the significant viscous entropy generation rates (*Su*) gradually expand to bulk contributions of cavity with the increase of *Pr*, thermal entropy generation rates (S_θ) and total entropy generation rates (S) mainly concentrate in the steepest temperature gradient, the entropy generation in the flow is dominated by heat transfer irreversibility and for the same Rayleigh number, the amplitudes of *Su*, S_θ and S decrease with increasing *Pr*. It is found that that the amplitudes of the horizontally averaged viscous entropy generation rates, thermal entropy generation rates and total entropy generation rates decrease with increasing *Pr*. The probability density functions of *Su*, S_θ and S also indicate that a much thinner tail while the tails for large entropy generation values seem to fit the log-normal curve well with increasing *Pr*. The distribution and the departure from log-normality become robust with decreasing *Pr*.

Keywords: entropy; Prandtl number; Rayleigh number; thermal; lattice Boltzmann method

1. Introduction

Natural convection heat transfer is widely applied in some important processes in engineering such as thermal storage, environmental comfort, grain drying, electronic cooling and other areas [1,2]. Rayleigh-Bénard (RB) convection is one of most classical natural convection in engineering. Several works with experimental [3–11] and numerical approaches [12–18] in various areas are available.Various Prandtl (*Pr*) numbers that range from $0(10^{-2})$ for mercury and molten metals to $0(10^4)$ for silicon oils have raised concern in various applications convection. The *Pr* values of 10^{23} in the viscous rocky part of the Earth's mantle further emerges in convection of planetary interiors. Thus, a systematic investigation of the dependence of the efficiency loss on the Prandtl number is worth performing. The process efficiency loss in all real processes can be closely related with the friction, mass transference, thermal gradients, chemical reactions, etc. Previous studies of entropy had emphasized potential advantages to evaluation of loss in engineering applications [13,14,19–22]. De reported the entropy generations due to heat and flow transport in the cavity and minimizing the entropy generation by using the second law of thermodynamics [13]. An optimal configuration with minimum loss of available energy may be gained using this method.

The importance of thermal boundary conditions in heat transfer processes and entropy generation characteristics inside a porous enclosure was investigated by Zahmatkesh [14]. To do this, a wide range of Darcy-modified Rayleigh numbers was analyzed by simulating the natural convection processes in a porous enclosure. Nayak [19] reported that combination of entropy generation with nanofluid-filled cavity block insertion. The thermodynamic optimization of the mixed convection were demonstrated by evaluating entropy generation and Bejan number. It is showed that the heat transfer rate increases remarkably by the addition of nanoparticles. The natural convection and entropy generation of nanofluid-filled cavities having different shaped obstacles with magnetic field effect was studied by Oztop [20]. It should be mentioned to this end the very good review paper on entropy generation in nanofluid flow by Mahian et al. [21]. A critical review of contributions to the theory and application of entropy generation analysis to different types of engineering systems was reported by Sciacovelli et al. [22]. The focus of the work is only on contributions oriented toward the use of entropy generation analysis as a tool for the design and optimization of engineering systems [22].

The main aim of the present work is the study of entropy generation in RB convection processes at different Prandtl numbers based on the minimal entropy generation principle by numerical simulation. The minimal entropy generation principle is that entropy generation in flow systems is associated with a loss of exergy. This is important, when exergy is used in a subsequent process and therefore its loss has to be minimized. The detailed information of local distributions of entropy generation due to frictional and heat transfer irreversibility at different Prandtl numbers as well as the overall entropy generation in the whole flow field are analyzed separately. All the numerical simulations have been implemented using a lattice Boltzmann scheme. Previous studies of the lattice Boltzmann method had emphasized potential advantages in a variety of single, multiphase and thermal fluid hydrodynamic problems [23–29]. Governing equations and numerical methods will be briefly described first in the following section. After that, the detailed numerical results and discussions are presented. Finally, some concluding remarks are provided.

2. Governing Equations and Numerical Method

2.1. Governing Equations

To study the dynamics of the fluid, the classical Oberbeck-Boussinesq (Ahlers et al. [8]; Lohse and Xia [6]) equations are adopted in this paper:

$$\frac{\partial \rho}{\partial t} + \nabla \cdot (\rho \mathbf{u}) = 0 \tag{1}$$

$$\frac{\partial (\rho \mathbf{u})}{\partial t} + \nabla \cdot (\rho \mathbf{u}\mathbf{u}) = -\nabla p + \nabla \cdot (2\rho\nu \mathbf{S}) - g\beta\Delta\theta \tag{2}$$

$$\frac{\partial \theta}{\partial t} + \mathbf{u} \cdot \nabla\theta = \kappa\nabla^2\theta \tag{3}$$

where ν and κ represent the kinematic viscosity and the diffusivity, respectively.

2.2. Entropy Generation

The amount of phenomenological information contained in the local entropy generation rates are studied by many researchers. As discussed in Bejan [30], Iandoli [31], Magherbi [32], Rejane [33], Mahian [21], Sheremet [34], Bhatt [35,36], Abbas [37] and Qing [38], etc., it is possible to derive an exact formula for both the viscous and the thermal components of the local entropy generation rates. In Cartesian notation of two-dimensional, the expressions are as follows:

$$S_u = \frac{\mu}{\theta}\left\{2\left[\left(\frac{\partial u}{\partial x}\right)^2 + \left(\frac{\partial v}{\partial y}\right)^2\right] + \left(\frac{\partial u}{\partial y} + \frac{\partial v}{\partial x}\right)^2\right\} \tag{4}$$

$$S_\theta = \frac{\kappa}{\theta^2}\left[(\frac{\partial\theta}{\partial x})^2 + (\frac{\partial\theta}{\partial y})^2\right] \tag{5}$$

and the total entropy generation rates can be given by:

$$S = S_u + S_\theta \tag{6}$$

Previous studies of the Bejan number (*Be*) had emphasized potential advantages to the importance of heat transfer irreversibility in the domain [39]. *Be* is proposed by Paoletti et al. [39]. Paoletti et al. investigated he contribution of heat transfer entropy generation on over all entropy generation by using the *Be*. *Be* is defined as:

$$Be = \frac{S_\theta}{S} \tag{7}$$

The range of *Be* is from 0 to 1. When *Be* is equal to 0, the irreversibility is dominated by fluid friction. Correspondingly, the irreversibility is dominated by heat transfer when *Be* is equal to 1. The irreversibility due to heat transfer dominates in the flow when *Be* is greater than 1/2. Correspondingly, *Be* < 1/2 implies that the irreversibilities due to the viscous effects dominate the processes. Meanwhile, it is also noted that the heat transfer and fluid friction entropy generation are equal in *Be* = 0.5 [39].

2.3. Numerical Method

Two simple lattice Bhatnagar-Gross-Krook (LBGK) collision operator are introduced. Specially, the evolution of LBGK is described by the following equation [27–29]:

$$f_i(x + c_i\Delta t, t + \Delta t) = f_i(x,t) + (f_i^{eq}(x,t) - f_i(x,t))/\tau_\nu + F_i \tag{8}$$

$$g_i(x + c_i\Delta t, t + \Delta t) = g_i(x,t) + (g_i^{eq}(x,t) - g_i(x,t))/\tau_\theta \tag{9}$$

where $f_i(x,t)$, $g_i(x,t)$ stand for the probability density functions to find at $(\mathbf{x}, t)$ a particle velocity belongs to a discrete and limited set c_i (with $i = 0, \cdots, 8$ in the $D2Q9$ adopted here).F_i is the discrete mesoscopic force corresponding with buoyant body force of Equation (2), τ_ν and τ_θ are the relaxation times for flow and temperature in lattice Boltzmann equations, respectively. The equilibrium function for the density distribution function is given as [28]:

$$f_i^{eq} = \rho w_i[1 + \frac{c_i \cdot u}{c_s^2} + \frac{(c_i \cdot u)^2}{c_s^4} - \frac{u^2}{2c_s^2}] \tag{10}$$

$$g_i^{eq} = \theta w_i[1 + \frac{c_i \cdot u}{c_s^2} + \frac{(c_i \cdot u)^2}{c_s^4} - \frac{u^2}{2c_s^2}] \tag{11}$$

where w_i is the associated weighting coefficient [23]. The kinematic viscosity ν and the diffusivity κ are given by:

$$\nu = \frac{2\tau_\nu - 1}{6}\frac{(\Delta x)^2}{\Delta t}, \kappa = \frac{2\tau_\theta - 1}{6}\frac{(\Delta x)^2}{\Delta t} \tag{12}$$

Density, momentum, and temperature are defined as coarse-grained (in velocity space) fields of the distribution functions:

$$\rho = \sum_{i=0}^{8} f_i,\ \rho u = \sum_{i=0}^{8} c_i f_i,\ \theta = \sum_{i=0}^{8} g_i, \tag{13}$$

A Chapman-Enskog expansion leads to the equations for density, momentum, and temperature from (8) and (9). To derive the classical Oberbeck-Boussinesq equations (Equations (1)–(3)), Two macroscopic time scales ($t_1 = \varepsilon t$, $t_2 = \varepsilon t$) and a macroscopic length scale ($x_1 = \varepsilon x$) are introduced. As for the FHP model two time scales and one spatial scale with $\partial t = \varepsilon\partial_{t1} + \varepsilon^2\partial_{t2}$ and $\partial_x = \varepsilon\partial_\alpha$ will be introduced. According to the above Chapman-Enskog expansion, the streaming step on the left-hand side reproduces the inertial terms in the classical Oberbeck-Boussinesq equations (Equations (1)–(3)).

Two important dimensionless parameters in RB convection are introducted in the following section. Ra is defined as $Ra = \beta\Delta\theta g H^3/\nu\kappa$. The enhancement of the heat transfer can be calculated by the *Nusselt* number $Nu = 1 + \langle u_y\theta\rangle/\kappa\Delta\theta H$ in the numerical results of LBM, where $\Delta\theta$ is the temperature difference between the bottom and top walls, H is the channel height, u_y is the vertical velocity, and $\langle . \rangle$ represents the average over the whole flow domain.

3. Simulation Results and Discussions

3.1. Analysis of S_u and S_θ

The entropy generation problem due to RB convection with various Pr in rectangular cavities is investigated. The incompressible, the Boussinesq approximation and the two-dimensional flow characteristics are implemented in the present paper. Schematic view of cavity is indicated in Figure 1. The grid verification of the results is inspected before the comparison. One example of the Rayleigh number of 5.4×10^9 is presented in Table 1. The number of grid points is taken the same in both the x and y directions in the present study. The size of grid points is taken as $N \times N$, in which N is the grid number in each spatial direction. It is shown that the calculated Nusselt number (Nu) changes with N. It is seen that when N increases, the Nu quickly approaches the benchmark result at Table 1. When N further increases from 2012 to 2400, not much improvement occurs for the result. So we can say that 2012×2012 lattices can give very accurate results for $Ra = 5.4 \times 10^9$.

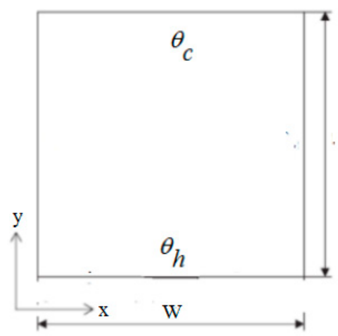

Figure 1. Schematic view of cavity.

Table 1. Grid verification for RB convection in a square cavity at $Ra = 5.4 \times 10^9$.

Mesh	600 × 600	1200 × 1200	2012 × 2012	2200 × 2200	2400 × 2400
Nu	683.23	693.08	697.35	697.36	697.36

Numerical simulations of two-dimensional RB convection at $Pr = 6$, 20, 100 and 10^6 are implemented by using LBM at $Ra = 5.4 \times 10^9$ in the present study. All two-dimensional simulations at different Pr are performed on 2012×2012 lattices. The no-slip boundary conditions are executed for top and bottom plates, which is same as left and right boundary condition in all simulations. The dimensionless initial temperature of bottom plates is equal to 1, and the dimensionless initial temperature of top plates is equal to 0. And the initial temperature between top and bottom plates is linear distribution from 0 to 1. When the heat flow about 2012×2012 lattice domain reaches steady state, CPU time of one case is 10 h by using the CPU of 16 cores.

Figure 2a–d show flow field and typical snapshots of the instantaneous temperature field obtained at four Prandtl number ($Pr = 6$, 20, 100, 10^6 and $Ra = 5.4 \times 10^9$). Blue (red) regions correspond to cold (hot) fluid. Large-scale circulations of the fluid are shaped, which develop mainly in the regions among the center of cavity at Figure 2a. And small vortex are emerged in four corners of square cavity, respectively. Large-scale circulations of the fluid in cavity are dissolved gradually with increasing *Pr*, which is similar to visualization of experiment for large *Pr* [6,11]. Large-scale structures of smaller thermal plumes gradually develop into rise and fall with increasing *Pr* from the bottom to top walls.

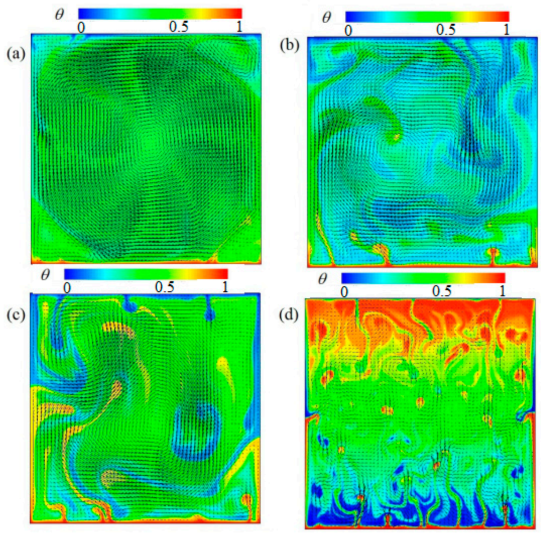

Figure 2. Flow field and temperature distributions at various Prandtl numbers from (**a**–**d**) (Pr = 6, 20, 100, 10^6 and $Ra = 5.4 \times 10^9$).

The corresponding logarithmic fields of viscous entropy generation rates S_u at four Prandtl number are shown in Figure 3a–d. From Figure 3a, it can be seen that the significant *Su* concentrates in the narrow region adjacent to the walls at Pr = 6, which is resulted from the steepest velocity gradient in the near-wall regions. It is observed that with the increase of *Pr*, the significant S_u gradually expands to bulk contributions of cavity from Figure 3b to Figure 3d, which is resulted from the steepest velocity gradient in the bulk of cavity.

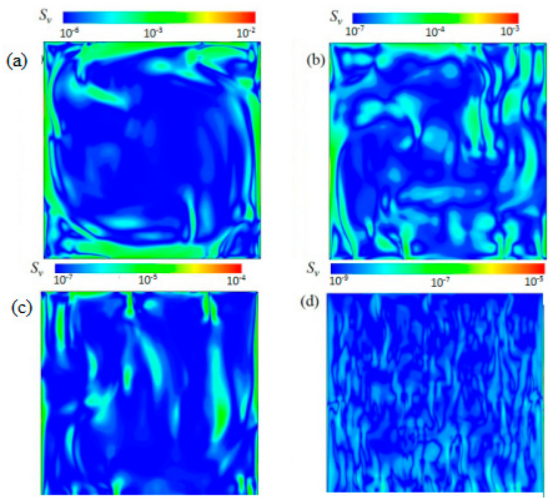

Figure 3. Viscous entropy generation rate at various Prandtl numbers from (**a**–**d**) (Pr = 6, 20, 100, 10^6 and $Ra = 5.4 \times 10^9$).

The distributions of thermal entropy generation rates S_θ for the four cases are shown in Figure 4. It is observed that the significant S_θ concentrates in the narrow region adjacent to the walls at Pr = 6 in Figure 4a, which is resulted from the steepest temperature gradient in the near-wall regions. From Figure 4b to Figure 4d, it is can be seen that the significant S_θ gradually expands to bulk contributions of cavity, which is resulted from the steepest temperature gradient in the bulk of the cavity.

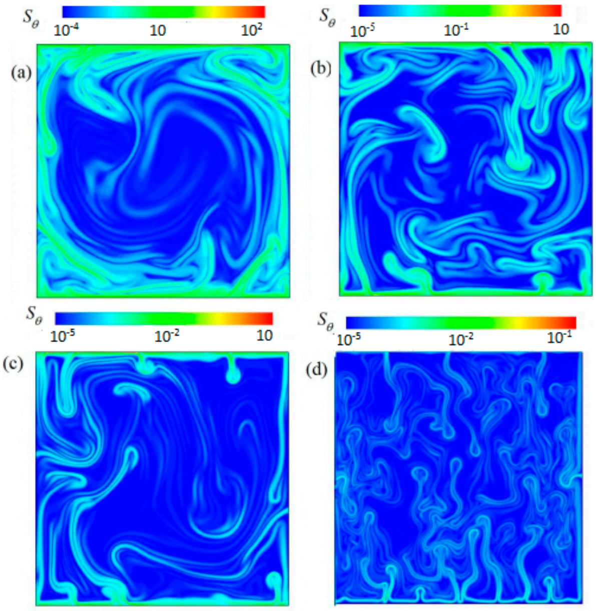

Figure 4. Thermal entropy generation rate at various Prandtl numbers from (**a**–**d**) (Pr = 6, 20, 100, 10^6 and $Ra = 5.4 \times 10^9$).

The corresponding logarithmic fields of the total entropy generation rates S are shown in Figure 5. Respectively, S is similar to the visualization of S_θ at the same Pr, which shows that the heat transfer dominates in the flow of cavity. Comparing Figures 3 and 4, it is noted that S_θ is much larger than S_u. This also indicates the entropy generation in the flow is dominated by heat transfer irreversibility. Moreover, one sees that the amplitudes of both S_u and S_θ decrease with increasing Pr.

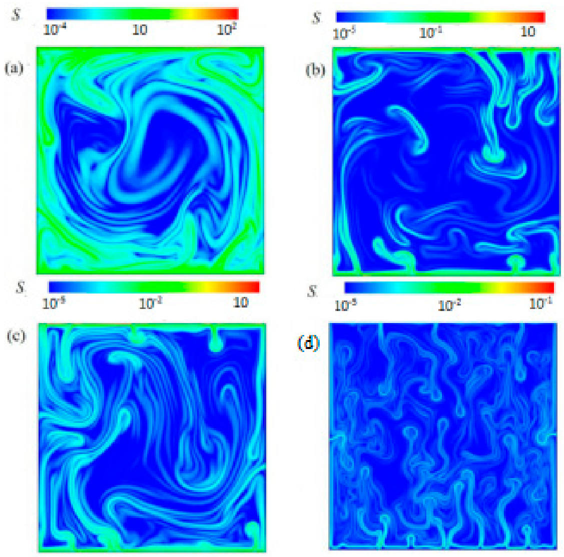

Figure 5. Total entropy generation rate at various Prandtl numbers from (**a**–**d**) (Pr = 6, 20, 100, 10^6 and $Ra = 5.4 \times 10^9$).

Figure 6 shows the distribution of Be at different Pr. For all cases, the values of Be in the region distributes in cavity, the region with Be greater than 0.5 distributes in the boundary layer and bulk contributions of cavity, which also indicates the entropy generation in the region is dominated by the heat transfer irreversibility.

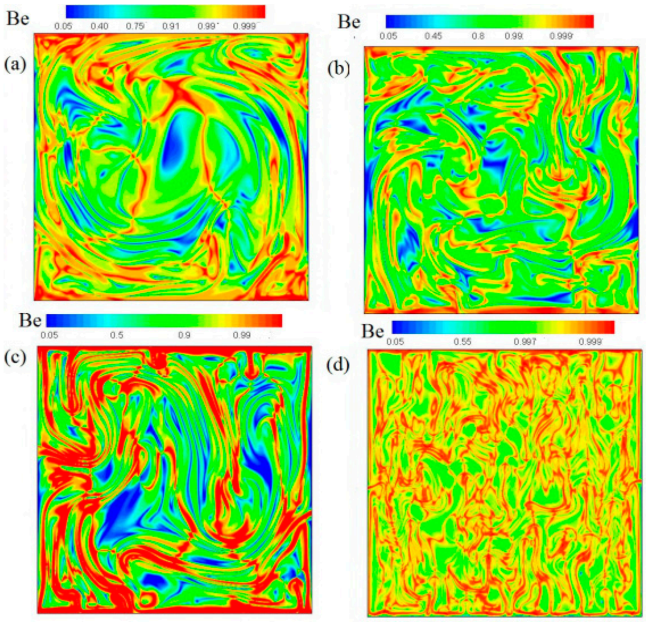

Figure 6. The contours of *Be* at various Prandtl numbers from (**a**–**d**) (Pr = 6, 20, 100, 10^6 and $Ra = 5.4 \times 10^9$).

3.2. Vertical Profiles of S_u and S_θ

Figure 7 displays the vertical profiles of the horizontally averaged viscous entropy generation rates $\langle S_u \rangle_x$ at various Pr. From Figure 7, it can be seen that the the horizontally averaged viscous entropy generation rates $\langle S_u \rangle_x$ of the top boundary layer and the bottom boundary layer is greater than the bulk contributions of cavity at various Pr, which is resulted from the steepest velocity gradient in the near-wall regions. Moreover, one sees that the amplitudes of the horizontally averaged viscous entropy generation rates $\langle S_u \rangle_x$ decrease with increasing Pr.

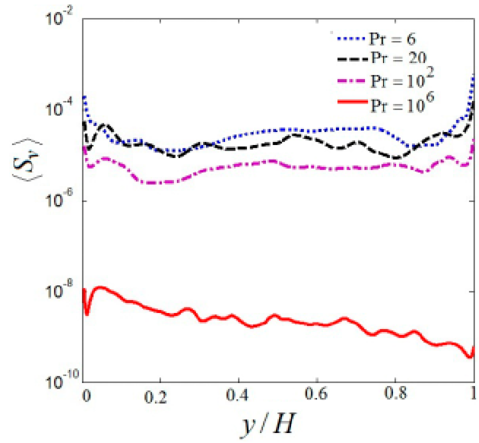

Figure 7. Mean vertical profiles of the the horizontally averaged viscous entropy generation rates $\langle S_u \rangle_x$ at various Prandtl numbers.

The vertical profiles of the horizontally averaged thermal entropy generation rates $\langle S_\theta \rangle_x$ is shown in Figure 8. Comparing Figures 7 and 8, it is noted that the horizontally averaged thermal entropy generation rates $\langle S_\theta \rangle_x$ is similar to the horizontally averaged viscous entropy generation rates $\langle S_u \rangle_x$. This also indicates that the horizontally averaged thermal entropy generation rates $\langle S_\theta \rangle_x$ of the top boundary layer and the bottom boundary layer is greater than bulk contributions of cavity at various *Pr*. Figure 9 shows the horizontally averaged total entropy generation rates $\langle S \rangle_x$, which is also similar to the horizontally averaged viscous entropy generation rates. Moreover, it is observed that the amplitudes of the horizontally averaged total entropy generation rates also decrease with increasing *Pr*.

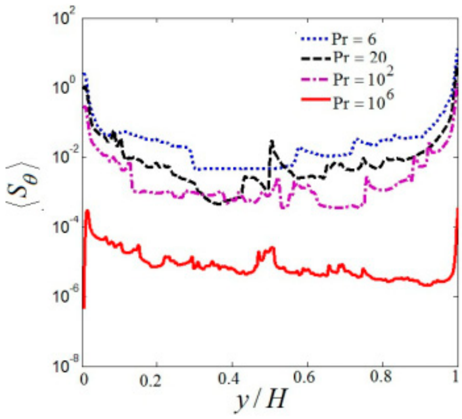

Figure 8. Mean vertical profiles of the the horizontally averaged thermal entropy generation rates $\langle S_\theta \rangle_x$ at various Prandtl numbers.

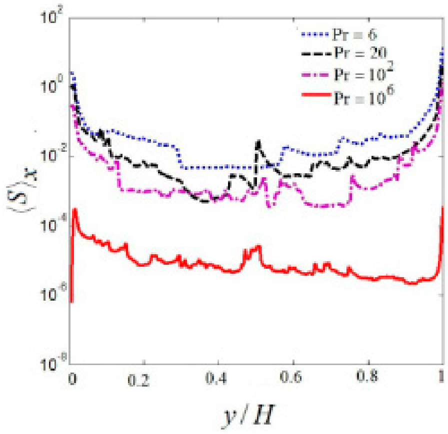

Figure 9. Mean vertical profiles of the the horizontally averaged total entropy generation rates $\langle S \rangle_x$ at various Prandtl numbers.

Figure 10 shows that the mean values of S_u, S_θ and S in the whole area versus *Pr*. It is observed that the mean values of S_u, S_θ and S in the whole area decrease with increasing *Pr* for the same Rayleigh number. It is also observed that the value of the thermal entropy generation is the two order of magnitude of viscous entropy generation, which also indicates the entropy generation in the flow is dominated by heat transfer irreversibility.

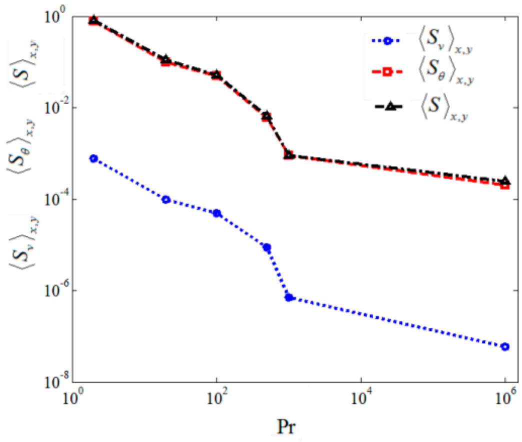

Figure 10. Mean values of S_u, S_θ and S in the whole area vs. Prandtl number.

3.3. Probability Density Functions (PDFs) of S_u and S_θ

Figures 11–13 plot the probability density functions (PDFs) of S_u, S_θ and S normalized by their respective rms value $(S_u)_{\mathrm{rms}} = \sqrt{\left\langle [S_u - \langle S_u \rangle_V]^2 \right\rangle_V}$, $(S_\theta)_{\mathrm{rms}} = \sqrt{\left\langle [S_\theta - \langle S_\theta \rangle_V]^2 \right\rangle_V}$, and $(S)_{\mathrm{rms}} = \sqrt{\left\langle [S - \langle S \rangle_V]^2 \right\rangle_V}$ at various Pr. Self-similarity of viscous entropy generation rates, thermal entropy generation rates and total entropy generation rates fluctuations is revealed by the observations that the PDFs obtained at distinct times collapse well on top of each other for S_u, S_θ and S. In addition, strong fluctuations for S_u, S_θ and S are revealed by the observations that the long tail of the calculated PDFs. In correspondence with the cases of both passive [40] and active scalars, a stretched exponential function is used to fit to the fraction of the PDF that extends from the most probable (mp) amplitude to the end of the tail. A stretched exponential function is given as:

$$p(Y) = \frac{C}{\sqrt{Y}} \exp(-mY^{\alpha}) \tag{14}$$

where C, m, and α are fitting parameters, and $Y = X - X_{\mathrm{mp}}$ with $X = S_u/(S_u)_{\mathrm{rms}}, S_\theta/(S_\theta)_{\mathrm{rms}}, S/(S)_{\mathrm{rms}}$ and X_{mp} being the abscissa of the most probable amplitude. The best fit of Equation (14) to the data yields m = 0.86 and α = 0.72 for S_u, m = 1.15 and α = 0.69 for S_θ and m = 1.06 and α = 0.72 for S. To highlight the differences in our present case for various Pr, we plot in Figure 11 the PDFs of S_u, in Figure 12 the PDFs of S_θ and in Figure 13 the PDFs of S in a log-log scale.

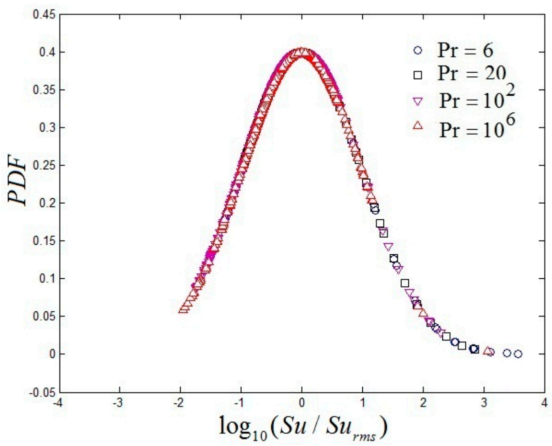

Figure 11. PDFs of viscous entropy generation rates S_u by their rms $(S_u)_{\mathrm{rms}}$ value.

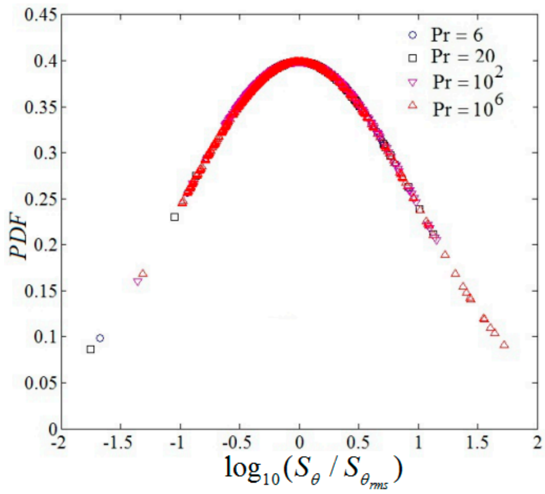

Figure 12. PDFs of thermal entropy generation rates S_θ by their rms $(S_\theta)_{\mathrm{rms}}$ value.

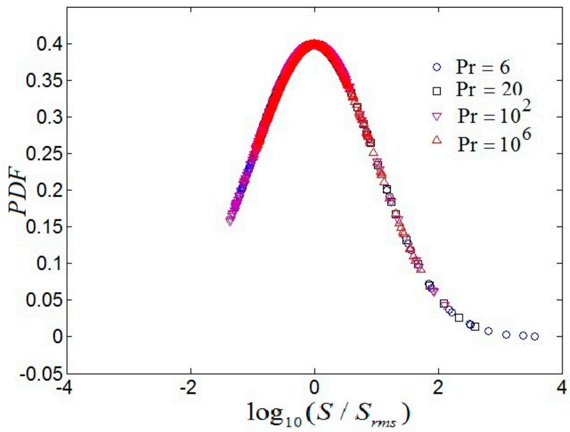

Figure 13. PDFs of total entropy generation rates S by their rms $(S)_{\mathrm{rms}}$ value.

The dashed lines in in Figures 11–13 indicate the log-normal distribution for comparison at various *Pr*. It is seen that for viscous entropy generation rates, thermal entropy generation rates and total entropy generation rates, small entropy generation values show a much thinner tail while the tails for large entropy generation values seem to fit the log-normal curve well with increasing *Pr*. The distribution and the departure from log-normality become robust within the self-similarity range with decreasing *Pr*.

4. Conclusions

The entropy generation for two-dimensional thermal convection at different *Pr* are investigated in the present study with LBM. Special attention is paid to analyze separately the detailed information of local distributions of entropy generation in virtue of frictional and heat transfer irreversibility and the overall entropy generation in the whole flow field. Several conclusions can be summarized.

Firstly, the significant S_u gradually expands to bulk contributions of cavity with the increase of *Pr*, which is resulted from the steepest velocity gradient in the bulk of cavity. S_θ and S mainly concentrate in the steepest temperature gradient in cavity.

In addition, the entropy generation in the flow heat transfer irreversibility plays an important role, frictional irreversibility can be neglected.

Thirdly, the amplitudes of S_u, S_θ and S decrease with increasing Pr for the same Rayleigh number. Further, the amplitudes of the horizontally averaged S_u, S_θ and S decrease with increasing Pr.

Finally, the PDFs of Su, S_θ and S obtained at various Pr indicate that with increase of Pr, the tails for large entropy generation values seem to fit the log-normal curve well while a much thinner tail. The distribution and the departure from log-normality become robust with decreasing Pr.

In this study it was possible to observe that the thermal and hydrodynamic problem is highly coupled. For a thermophysical configuration involving thermal convection, the larger Pr are the better option. Increasing Pr increase the systems efficiency. This different Pr and thermophysical configuration could be applied, for example, in technical applications convection is characterized by very different Pr, ranging from $0(10^{-2})$ for mercury and molten metals to $0(10^{4})$ for silicon oils.

Acknowledgments: This work was supported by the Young Researchers Foundation of Zhejiang Provincial Top Key Academic Discipline of Mechanical Engineering, the National Natural Science Foundation of China (51536008, 91441104 and 11502237), Zhejiang Province Science and Technology Innovation Team Project (2013TD18) and the Department of Education Project of Zhejiang Province (No. Y201534610). The authors appreciate sincerely the referees valuable comments and suggestions on our work.

Author Contributions: The authors contributed equally to this work.

Conflicts of Interest: The authors declare no conflict of interest.

References

1. Lage, J.L.; Lim, J.S.; Bejan, A. Natural convection with radiation in a cavity with open top end. *J. Heat Transf.* **1992**, *114*, 479–486. [CrossRef]
2. Khaled, A.S. Natural convection coupled with radiation heat transfer in an inclined porous cavity with corner heater. *Comput. Fluids* **2014**, *102*, 74–84.
3. Nelson, J.E.; Balakrishnan, A.R.; Murthy, S.S. Experiments on stratified chilled-water tanks. *Int. J. Refrig.* **1999**, *22*, 216–234. [CrossRef]
4. Ampofo, F.; Karayiannis, T.G. Experimental benchmark data for turbulent natural convection in an air filled square cavity. *Int. J. Heat Mass Transf.* **2003**, *46*, 3551–3572. [CrossRef]
5. Adeyinka, O.B.; Naterer, G.F. Experimental uncertainty of measured entropyproduction with pulsed laser PIV and planar laser induced fluorescence. *Appl. Therm. Eng.* **2005**, *48*, 1450–1461.
6. Lohse, D.; Xia, K.Q. Small-scale properties of turbulent Rayleigh-Bénard convection. *Annu. Rev. Fluid Mech.* **2010**, *42*, 335–364. [CrossRef]
7. Chilla, F.; Schumacher, J. New perspectives in turbulent Rayleigh-Bénard convection. *Eur. Phys. J. E* **2012**, *35*, 58–82. [CrossRef] [PubMed]
8. Ahlers, G.; Grossmann, S.; Lohse, D. Heat transfer and large scale dynamics in turbulent Rayleigh-Bénard convection. *Rev. Mod. Phys.* **2009**, *81*, 503–537. [CrossRef]
9. Sun, C.; Zhou, Q.; Xia, K.Q. Cascades of velocity and temperature fluctuations in buoyancy-driven thermal turbulence. *Phys. Rev. Lett.* **2006**, *97*, 144504. [CrossRef] [PubMed]
10. Zhou, Q.; Xia, K.Q. Aspect ratio dependence of heat transport by turbulent Rayleigh-Bénard convectin in rectangular cells. *J. Fluid Mech.* **2011**, *710*, 260–276. [CrossRef]
11. Zhou, Q.; Xia, K.Q. Physical and geometrical properties of thermal plumes in turbulent Rayleigh-Bénard convection. *New J. Phys.* **2012**, *12*, 075006. [CrossRef]
12. Poujol, F.T. Natural convection of a high *Prandtl* number fluid in cavity. *Int. Commun. Heat Mass Transf.* **2000**, *27*, 109–118. [CrossRef]
13. De, R.; Oliveski, C.; Krenzinger, A.; Vielmo, H.A. Cooling of cylindrical vertical tank submitted to natural internal convection. *Int. J. Heat Mass Transf.* **2003**, *46*, 2015–2026.
14. Zahmatkesh, I. On the importance of thermal boundary conditions in heat transfer and entropy generation for natural convection inside a porous enclosure. *Int. J. Therm. Sci.* **2008**, *47*, 339–346. [CrossRef]
15. Andreozzi, A.; Auletta, A.; Manca, O. Entropy generation in natural convection in a symmetrically and uniformly heated vertical channel. *Int. J. Heat Mass Transf.* **2006**, *49*, 3221–3228. [CrossRef]
16. Dagtekin, I.; Oztop, H.F.; Bahloul, A. Entropy generation for natural convection in C-shaped enclosures. *Int. Commun. Heat Mass Transf.* **2007**, *34*, 502–510. [CrossRef]

17. Shishkina, O.; Wagner, C. Analysis of sheet like thermal plumes in turbulent Rayleigh-Bénard convection. *J. Fluid Mech.* **2012**, *599*, 383–404. [CrossRef]
18. Kaczorowski, M.; Wagner, C. Analysis of the thermal plumes in turbulent Rayleigh-Bénard convection based on well-resolved numerical simulations. *J. Fluid Mech.* **2011**, *618*, 89–112. [CrossRef]
19. Nayak, R.K.; Bhattacharyya, S.; Pop, I. Numerical study on mixed convection and entropy generation of Cu-water nanofluid in a differentially heated skewed enclosure. *Int. J. Heat Mass Transf.* **2015**, *85*, 620–634. [CrossRef]
20. Selimefendigil, F.; Öztop, H.F. Natural convection and entropy generation of nanofluid filled cavity having different shaped obstacles under the influence of magnetic field and internal heat generation. *J. Taiwan Inst. Chem. Eng.* **2015**, *56*, 42–56. [CrossRef]
21. Mahian, O.; Kianifar, A.; Pop, I. A review on entropy generation in nanofluid flow. *Int. J. Heat Mass Transf.* **2013**, *65*, 514–532. [CrossRef]
22. Sciacovelli, A.; Verda, V.; Sciubba, E. Entropy generation analysis as a design tool—A review. *Renew. Sustain. Energy Rev.* **2015**, *43*, 1167–1181. [CrossRef]
23. Qian, Y.H.; D'Humieres, D.; Lallemand, P. Lattice BGK Models for Navier-Stokes Equation. *Europhys. Lett.* **1992**, *17*, 479–484. [CrossRef]
24. Chen, S.Y.; Doolen, G.D. Lattice Boltzmann method for fluid flows. *Annu. Rev. Fluid Mech.* **1998**, *30*, 329–364. [CrossRef]
25. Aidun, C.K. Lattice-Boltzmann Method for Complex Flows. *Annu. Rev. Fluid Mech.* **2010**, *42*, 439–472. [CrossRef]
26. Shan, X. Simulation of Rayleigh-Bénard convection using a lattice Boltzmann method. *Phys. Rev. E* **1997**, *55*, 2780–2788. [CrossRef]
27. He, X.; Chen, S.; Doolen, G.D. A novel thermal model for the lattice Boltzmann method in incompressible limit. *J. Comput. Phys.* **1998**, *146*, 282–300. [CrossRef]
28. Wei, Y.K.; Wang, Z.D.; Yang, J.F.; Dou, H.S.; Qian, Y.H. Simulation of natural convection heat transfer in an enclosure using lattice Boltzmann method. *Comput. Fluids* **2016**, *124*, 30–38. [CrossRef]
29. Wei, Y.K.; Dou, H.S.; Yang, H. Characteristics of heat transfer with different dimensionless distance in an enclosure. *Mod. Phys. Lett. B* **2016**, *30*, 1650364–1650369. [CrossRef]
30. Bejan, A. *Entropy Generation through Heat and Fluid Flow*; John Wiley & Sons: New York, NY, USA, 1982.
31. Iandoli, C.L. Analysis of the Entropy Generation Fields of a Low n_s Centrifugal Compressor. Master's Thesis, University of Rome, Rome, Italy, 2000. (In Italian)
32. Magherbi, M.; Abbassi, H.; Brahim, A.B. Entropy generation at the onset of natural convection. *Int. J. Heat Mass Transf.* **2003**, *46*, 3441–3450. [CrossRef]
33. Rejane, D.C.; Mario, H.; Copetti, J.B. Entropy generation and natural convection in rectangular cavities. *Appl. Therm. Eng.* **2009**, *29*, 1417–1425.
34. Sheremet, M.A.; Oztop, H.F.; Pop, I.; Hamdeh, N.A. Analysis of Entropy Generation in Natural Convection of Nanofluid inside a Square Cavity Having Hot Solid Block: Tiwari and Das'Model. *Entropy* **2016**, *18*, 9. [CrossRef]
35. Bhatti, M.M.; Abbas, T.; Rashidi, M.M.; Ali, M.E.; Yang, Z.G. Entropy Generation on MHD Eyring-Powell Nanofluid through a Permeable Stretching Surface. *Entropy* **2016**, *18*, 224. [CrossRef]
36. Bhatti, M.M.; Rashidi, M.M. Entropy generation with nonlinear thermal radiation in MHD boundary layer flow over a permeable shrinking/stretching sheet: Numerical solution. *J. Nanofluids* **2016**, *5*, 543–554. [CrossRef]
37. Abbas, M.A.; Bai, Y.; Rashidi, M.M.; Bhatti, M.M. Analysis of Entropy Generation in the Flow of Peristaltic Nanofluids in Channels with Compliant Walls. *Entropy* **2016**, *18*, 90. [CrossRef]
38. Qing, J.; Bhatti, M.M.; Abbas, M.A.; Rashidi, M.M.; Ali, M.S. Entropy Generation on MHD Casson Nanofluid Flow over a Porous Stretching/Shrinking Surface. *Entropy* **2016**, *18*, 123. [CrossRef]

39. Paoletti, S.; Rispoli, F.; Sciubba, E. Calculation of exergetic losses in compact heat exchanger passages. *ASME AES* **1989**, *10*, 21–29.
40. Schumacher, J.; Sreenivasan, K.R. Statistics and geometry of passive scalars in turbulence. *Phys. Fluids* **2005**, *17*, 125107. [CrossRef]